



TECHNICAL ARTICLE

Microstructure and Mechanical Properties of Welded Joints of Stainless Steel Clad Sheets Using Cr-Ni-Cu-Al Multi-Principal Filler Wires

Dejia Liu, Xuean Zha, WeiXiong Wang, Yanchuan Tang, Haitao Jiao, Yong Hu, Longzhi Zhao, and Jian Zhang

Submitted: 26 April 2022 / Revised: 19 June 2022 / Accepted: 29 June 2022 / Published online: 7 October 2022

High-entropy alloys (HEAs), with the promising properties of high strength/hardness, excellent corrosion, and oxidation resistance, have a broad application prospect in the welding field. Owing to the cocktail effect of HEAs, the mechanical properties of welded joints could be improved by the composition change and alloying of multi-principal filler materials. In the present study, the joining of commercial 304/Q235 stainless steel clad sheets was taken as the research object. Three types of Cr-Ni-Cu-Al multi-principal filler wires with different Al content were designed, to study the influence of Al content on the microstructure and properties of welded joints. It was found that the grain morphologies in the weld zones were significantly changed from columnar/dendritic grains to spinodal decomposition structures, with the increase in Al content in the filler wires. The phase structures were converted from a face-centered cubic (FCC) phase into the body-centered cubic (BCC) + FCC phases. A finding was that the ultimate tensile strength of the joints was improved from ~ 379 to ~ 528 MPa, as the Al content in the filler wires was increased from 10 to 26 at.%. The hardness in the weld zones was increased by ~ 2 times. The research results could provide experimental references to modify the joint performance by using filler materials with multi-principal elements.

Keywords hardness, microstructures, multi-principal filler materials, stainless steel clad sheets, tensile properties

1. Introduction

As new developing advanced materials, high-entropy alloys (HEAs) have the high-entropy effect, severe-lattice-distortion effect, and sluggish diffusion effect, by incorporating five or more principal elements (Ref 1-3). Promising properties of high strength, excellent corrosion, and oxidation resistance could be potentially performed in HEAs (Ref 4, 5). With the growth in the interest and research on HEAs, the application of HEAs in the welding field has attracted scholarly attention (Ref 6-8). Many scholars have studied the weldability of HEAs or dissimilar welding between HEAs and other metals (Ref 9-15). In addition, using HEAs as filler materials to modify the microstructure in weld zones (WZs) and improve the mechan-

ical properties of welded joints has been reported in previous studies (Ref 16-18). For example, the dissimilar joining of TC4 alloy to 304 stainless steel was successfully achieved by using $(\text{CoCrFeNi})_{100-x}\text{Cu}_x$ HEAs as interlayer materials (Ref 19). Moreover, the joining of stainless steel to carbon steel, or to Al alloy has been achieved by using multi-principal mixed powders as filler materials (Ref 20-22). Therefore, it is meaningful to adopt high-entropy materials as filler materials to improve joint performances.

Due to the cocktail effect, it has a close relationship between the properties and the constituent elements of HEAs (Ref 23-25). It is expected to control the properties of HEAs by the composition change and alloying. As is known, due to the differences in slip system, slip direction, and stacking fault energy between face-centered cubic (FCC) and body-centered cubic (BCC) structures, the plasticity of the BCC structure is weaker than that of FCC structure in general. And compared with FCC solid-solution phase, BCC solid-solution phase can improve hardness and reduce the plasticity of HEAs (Ref 19, 26). Moreover, by increasing the content of BCC-forming elements, the formation of BCC structures can be promoted, and then the hardness of HEA can be improved. Therefore, it is generally accepted that BCC-forming elements lead to hardness improvement and plasticity reduction in HEAs, while FCC-forming elements cause the hardness reduced and the plasticity/elasticity improved (Ref 26). The mechanical properties of HEAs are severely affected by the ratio of FCC- and BCC-forming elements (Ref 27, 28). For example, attributed to the high content of FCC-forming element of Ni, increasing plastic strain and decreasing yield strength were observed in $\text{CoFeNi}_x\text{VMo}_y$ alloys (Ref 29). Recently, Liu et al. (Ref 20) reported that the hardness, tensile, and bending properties of the

Dejia Liu, Yanchuan Tang, Haitao Jiao, Yong Hu, Longzhi Zhao, and Jian Zhang, School of Materials Science and Engineering, East China Jiaotong University, Shuang Gang Dong Jie 808#, Economic and Technological Development Zone, Nanchang 330013, China; and Nanchang Key Laboratory of Advanced Materials and Laser Additive Manufacturing for Vehicles, Nanchang 330013, China; and Xuean Zha and WeiXiong Wang, School of Materials Science and Engineering, East China Jiaotong University, Shuang Gang Dong Jie 808#, Economic and Technological Development Zone, Nanchang 330013, China. Contact e-mails: ldj515@126.com and zhaolongzhi@163.com.

welded joints are severely affected by an elemental composition factor of λ , for the $(\text{CrMnFe})_x(\text{CoNi})_y$ powders, ($\lambda = x/y$). It was found that BCC-forming elements promote the generation of BCC structure and increase the hardness in the WZs. It is of great significance to modify the mechanical properties of welded joints by the composition change and alloying of multi-principal filler materials.

Recently, it is widely reported that the Al content can affect the mechanical properties of HEAs. Xu et al. (Ref 30) found that increasing Al content in $\text{Al}_x\text{CrMnFeCoNi}$ alloys can increase the volume fraction of the BCC phase and result in remarkably improved tensile strength. Wang et al. (Ref 31) reported that owing to the dramatic refinement of microstructures, the yield strength of $\text{Ni}_{1.5}\text{CoFeCu}_{1-x}\text{Al}_x\text{V}_{0.5}$ alloys is significantly enhanced as an increase in Al content. However, the effects of Al content in multi-principal filler materials on the microstructure and properties of the welded joints have not yet been studied. As is known, Fe, Co, Cr, Ni, Cu, and Al are common principal elements for HEAs (Ref 32). However, as the main element of steel, Fe element can be introduced into the weld pool during the welding process due to the melting of steel base metal (BM), which may result in excessive Fe element in WZ. The chemical composition in WZ may deviate from the range of HEA (5-35 at.%). Therefore, the Fe element is excluded from the design of filler materials in this study. Moreover, cobalt is a precious metal. The raw material of pure Co has a high price. To reduce the cost of filler materials and consider the engineering application, the Co element is also excluded from the designed filler materials. Finally, three types of Cr-Ni-Cu-Al multi-principal alloy wires with different Al content were designed as filler materials.

Stainless steel clad sheets are widely used in the fields of chemical industry, navigation, and petroleum vessel (Ref 33-35). The welded joints of stainless steel clad sheets usually need to have promising mechanical properties and corrosion resistance. Due to the significant differences in chemical compositions between the flyer layer and the base layer, element migration of C, Cr, and Ni elements is commonly observed in the WZ of stainless steel clad sheets (Ref 33, 36). The welded joints by using steel-based filler materials show insufficient corrosion resistance due to the high content of the C element in the WZ. Moreover, martensite structures are easily formed in the WZ, which may lead to joint embrittlement (Ref 34). The welded joints by using Ni-based filler materials can present a favorable corrosion resistance. However, the joint mechanical properties can be further improved (Ref 34, 36). High-entropy filler materials may achieve the welded joints showing promising corrosion resistance and mechanical properties. Therefore, the commercial 304/Q235 stainless steel clad sheets are taken as the BM. The effects of Al content in multi-principal alloy wires on the microstructure, hardness, and tensile properties of the stainless steel clad joints are explored. To a certain degree, the research results provide experimental references to modify the joint performance by using filler materials with multi-principal elements.

2. Experimental

The 304/Q235 stainless steel clad sheets were taken as the research object. The thicknesses of the 304 flyer layer, and Q235 base layer were about 1 mm and 2 mm, respectively. To

reduce the weld dilution, a 90° V-shape groove with the root of the groove on the Q235 base layer was processed. A 1-mm wide gap was reserved at the root of the groove before welding. Cu, Al pure wires with a purity of more than 99.95 wt.% and Ni80Cr20 alloy wires, with a diameter of 0.5 mm, were utilized to manufacture the Cr-Ni-Cu-Al multi-principal alloy wires by mechanical winding. To comparatively analyze the effects of Al content in the multi-principal alloy wires on the microstructure and joint properties, three types of multi-principal alloy wires were designed through the various amounts of Al wires. The amount of Al pure wires was included from one, two, and three for the multi-principal alloy wires while keeping the constant amount of other pure or alloy wires. The theoretical chemical compositions of those multi-principal alloy wires are shown in Table 1.

The welded joints by using the multi-principal alloy wires with single, double, and triple Al wires were named Sample 1, Sample 2, and Sample 3, respectively. Tungsten inert gas shielded welding (TIG-Welding, JASIC WSE315P) was applied to finish the joining of 304/Q235 stainless steel clad sheets by using the Cr-Ni-Cu-Al multi-principal alloy wires. After process optimization, the welding parameters with a current of 67 A, a 2-mm diameter tungsten needle, and the purity of 99.99% Ar gas with a flow of 15L/min were determined. After welding, metallographic samples were cut on the cross section of WZ. The metallographic samples were polished and then corroded by using two steps. Firstly, a 4 vol.% nitric acid alcohol solution was used to etch the Q235 base layer. Secondly, aqua-regia was used to etch the 304 flyer layer and WZs. Stereomicroscope (Zeiss Stemi-508), optical microscopy (Zeiss Axio Vert.A1), and scanning electron microscope (SEM, Hitachi SU8010) were employed to examine the macro-morphologies and microstructures of the welded joints. The elemental composition of the welded joints was determined by using a Bruker Xflash 6160 energy dispersive spectrometer (EDS) equipped with the SEM. The phases of the WZs were examined by X-ray diffractometer (XRD, Shimadzu XRD-6100) using a Cu $K\alpha$ target. A Vickers microhardness tester (HV1000IS) was used to analyze the hardness, with a load of 200 g and a dwell time of 10 s. The tensile tests were carried out at the temperature of 25 °C by using dumbbell-shaped tensile specimens (16 mm \times 5 mm \times 3 mm). The tensile rate is $1 \times 10^{-3} \text{ s}^{-1}$. To assure representative results, three tensile specimens for each welded joint were tested.

3. Results

3.1 Microstructures of the Weld Interfaces

Figure 1 shows that three types of welded joints are fully penetrated. Weld defects including cracks and pores have not

Table 1 Chemical composition of three types of filler materials, at.%

	Cr	Ni	Cu	Al
Sample 1	14	47	29	10
Sample 2	12	43	26	19
Sample 3	11	39	24	26

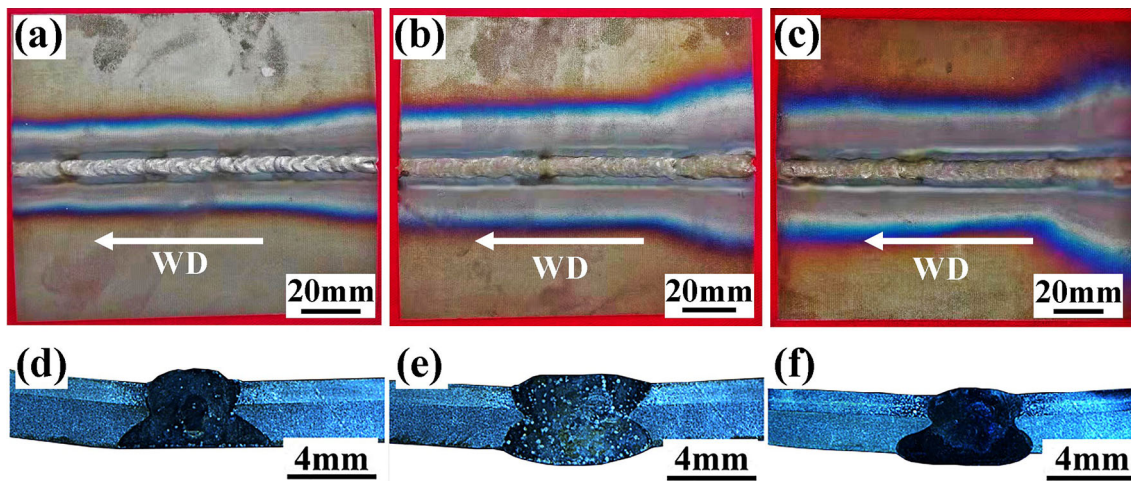


Fig. 1 Macroscopic appearances of various welded joints: (a, d) Sample 1; (b, e) Sample 2; (c, f) Sample 3

been seen on the cross-sections of the welded joints. It means that the 304/Q235 stainless steel clad sheets are successfully welded by using the Cr-Ni-Cu-Al multi-principal alloy wires. Moreover, the heat-affected zones (HAZs) are observed close to the WZs in the macroscopic appearances (see Fig. 1a-c). Moreover, the width of the HAZ in the transverse direction (TD) seems to be larger on the edges of the arc starting segment, compared to the arc stabilization stage and arc ending segment. As is known, in the TIG-Welding process, to maintain the shape of the WZ, the wire feeding speed in the arc starting stage is slow, and the arc dwell time is long (Ref 37). This may be the main reason for the larger HAZ on the edges of the arc starting segment. Figure 1(d), (e) and (f) showed the macroscopic appearances of the cross section of WZs. Based on the area of the cross section of WZs, as well as the shape and size of the groove and the assembly gap, the dilution rate of three types of WZs is measured. It is found that the highest dilution rate is observed in Sample 2 ($\sim 45.5\%$), while the dilution rate of Sample 1 is $\sim 22.3\%$, and that of Sample 3 is $\sim 39.4\%$. It should be noted that the dilution rate in this study is higher than that in previous studies using the TIG-Welding process (Ref 38). Moreover, Marangoni currents are observed on the cross section images of three types of WZs, which have been widely found in previous studies, especially for the joints by fusion welding of dissimilar materials or layered heterogeneous clad sheets (Ref 39, 40). Based on previous studies (Ref 39, 40), the Marangoni effect can result in a complex flow pattern as well as the material flow traces on the cross section of WZs.

The microstructures in the regions near the BM/WZ interfaces are shown in Fig. 2. Clear boundaries are observed between the BMs and WZs for three types of samples. Typical columnar grains are observed in the WZs near the BM/WZ interfaces. Owing to the directional heat dissipation in the molten pool during the welding process (Ref 41), the columnar grains tend to grow in the vertical direction of the edge of the molten pool. Large differences in thermophysical parameters exist between the 304 flyer layer, Q235 base layer, and the filler materials, which have an impact on the microstructure evolution in the WZs as well as the HAZ. For example, it is measured that the primary arm spacing of columnar grains in the WZ on the 304 flyer layer for Sample 1 (see Fig. 2a) is $36.1 \pm 4.5 \mu\text{m}$, while that on the Q235 base layer (see Fig. 2d) is $18.5 \pm 6.3 \mu\text{m}$. The columnar grains in the former are much

coarser than that of the latter. The reason is mainly attributed to the lower thermal conductivity of 304 stainless steel than Q235 steel (Ref 20). Moreover, coarse austenite grains are observed in the HAZ of the 304 flyer layer (see Fig. 2a-c), while the black pearlite is seen in the HAZ of Q235 base layer. In addition, the morphologies of the WZ in Sample 3 are much darker than those of Samples 1 and 2 based on the optical microscope (OM) images. As is known, the region with good corrosion resistance may show a white morphology, while the region with poor corrosion resistance may show a black morphology in OM images. As stated above, aqua-regia is used for etching three types of WZs. Therefore, it means that the WZ in Sample 3 seems to have poorer corrosion resistance in aqua-regia compared to that of the other two samples. The results may have a close relationship with the different chemical compositions and phase structures in those WZs.

The chemical composition variability near the BM/WZ interfaces on the Q235 base layer is evaluated. The white arrows in Fig. 3(a), (b) and (c) indicate the measured paths of elemental line scanning. The results in Fig. 3(d), (e) and (f) indicate that the content of Fe element has remarkably decreased from the BM of Q235 steel to the WZs, while the contents of other elements, including Cr, Ni, Cu, and Al, are significantly increased in the WZs. Figure 3(d) indicates that the mean atomic ratio of Fe: Ni: Cr: Al: Cu is approximately 44.3: 17.7: 19.6: 9.9: 8.4 in the WZ closing to the BM/WZ interface of Sample 1. It should be noted that Fe element is excluded from the filler materials in this study. However, the high content of Fe element is observed in the WZ for Sample 1. The reason is mainly attributed to the melted BM during the welding process, resulting in a large amount of Fe introduced into the molten pool, especially in the regions close to the BM/WZ interface. In addition, apparent differences in the composition of elements are observed in another two WZs. For Sample 2, the mean atomic ratio of each element in the WZ near the BM/WZ interface is Fe: Ni: Cr: Al: Cu = 49.2: 13.4: 17.1: 13.8: 6.6. The atomic ratio of each element in the WZ of Sample 3 is Fe: Ni: Cr: Al: Cu = 29: 18.9: 14.4: 27.3: 10.5. Gradually increased Al contents are found in those WZs from Sample 1 to Sample 3. In addition, the amount of each element in the WZ of Sample 3 is located in the range of 10 \sim 30 at.%, which is well-consistent with the definition of HEAs (Ref 32, 42).

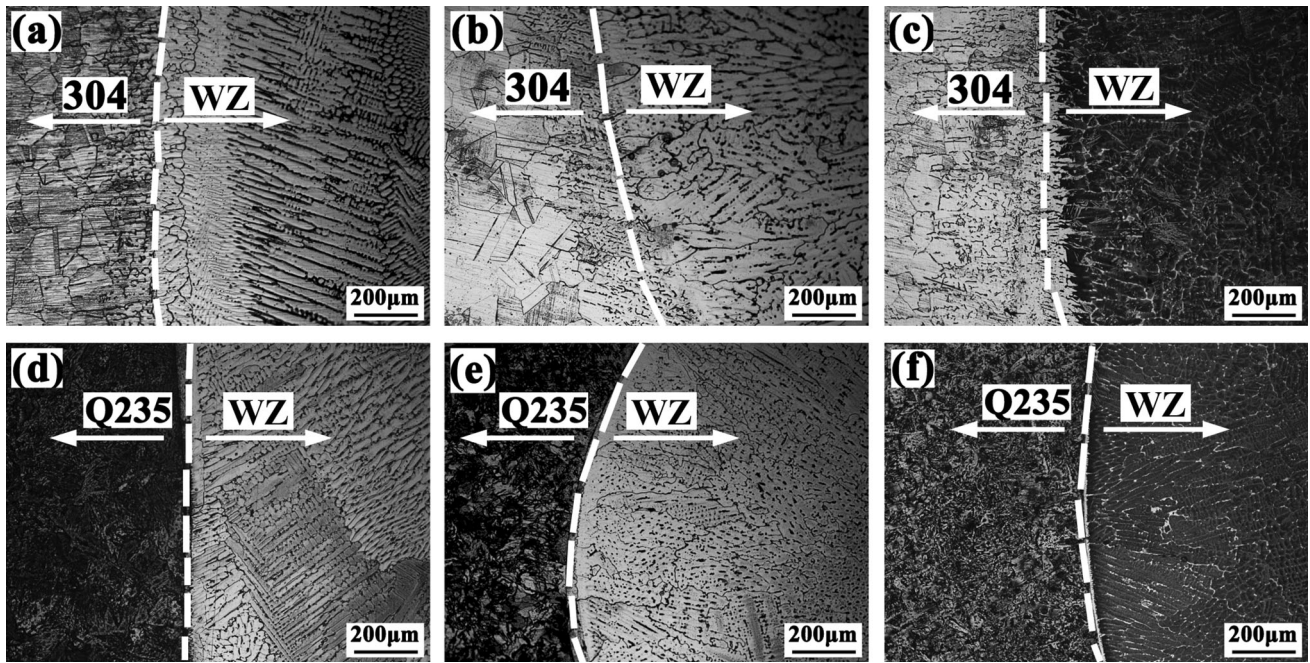


Fig. 2 Microstructures evolution of the WZ/BM interface of various welded joints: (a, d) Sample 1; (b, e) Sample 2; (c, f) Sample 3

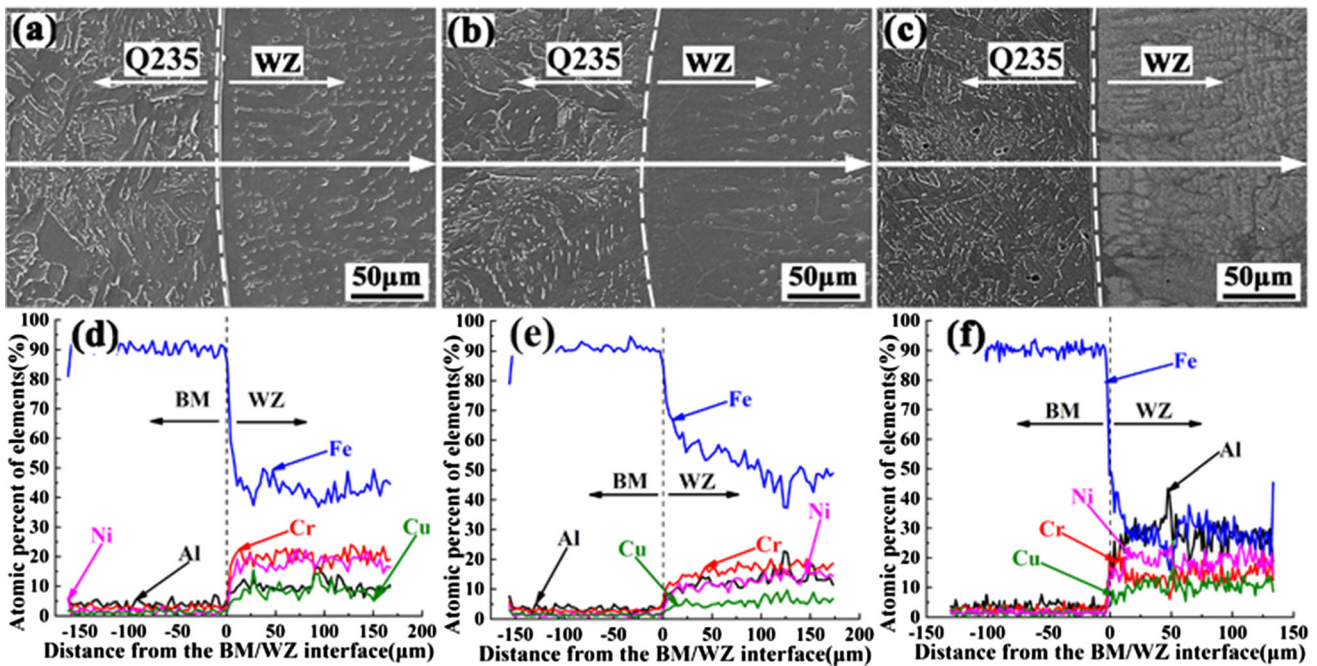


Fig. 3 SEM and EDS line analysis of the WZ/BM interface of various welded joints: (a, d) Sample 1; (b, e) Sample 2; (c, f) Sample 3

3.2 Microstructures of the WZs

Figure 4 presents the microstructure evolution of WZ for Sample 1. The cross section of the WZ at low magnification is provided at the top of Fig. 4. The various morphologies in different regions of WZ are sequentially presented in Fig. 4(a), (b), (c) and (d). Figure 4(a) shows that columnar grains are observed in the WZ on the left side, which is near the BM/WZ interface. Based on experimental observation, the width of the regions consisting of columnar grains is $\sim 300 \mu\text{m}$ in the TD. The primary arm spacing of columnar grains in the WZ on the

left side (see Fig. 4a) is $\sim 36.5 \pm 3.1 \mu\text{m}$. Then, as the region is close to the center of the WZ, equiaxed dendritic grains and fine columnar grains are observed in most regions of the WZ (see Fig. 4b and c). Figure 4(d) presents that fine columnar grains are found on another side of the WZ. It is measured that the primary arm spacing of columnar grains in the WZ on the right side (see Fig. 4d) is $\sim 11.2 \pm 5.1 \mu\text{m}$. Moreover, a small number of equiaxed dendritic grains are observed between columnar and dendritic grains in Fig. 4(d). To observe more details of the equiaxed dendritic grains, the SEM image of the equiaxed dendritic grains in the WZ of Sample 1 is presented in

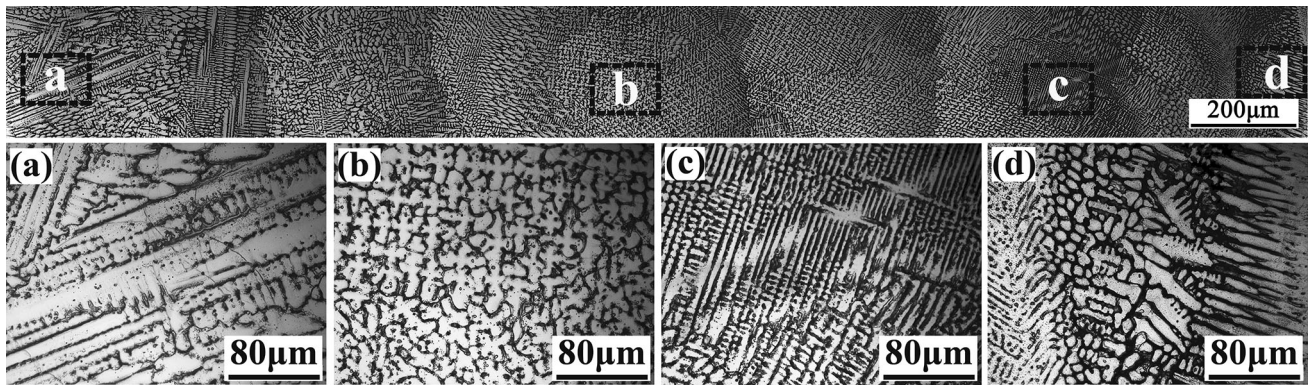


Fig. 4 Microstructures evolution of the WZ of Sample 1: (a) columnar grains in the WZ on the left side; (b, c) equiaxed dendritic grains and fine columnar grains in most regions of the WZ; (d) fine columnar grains in the WZ on the right side

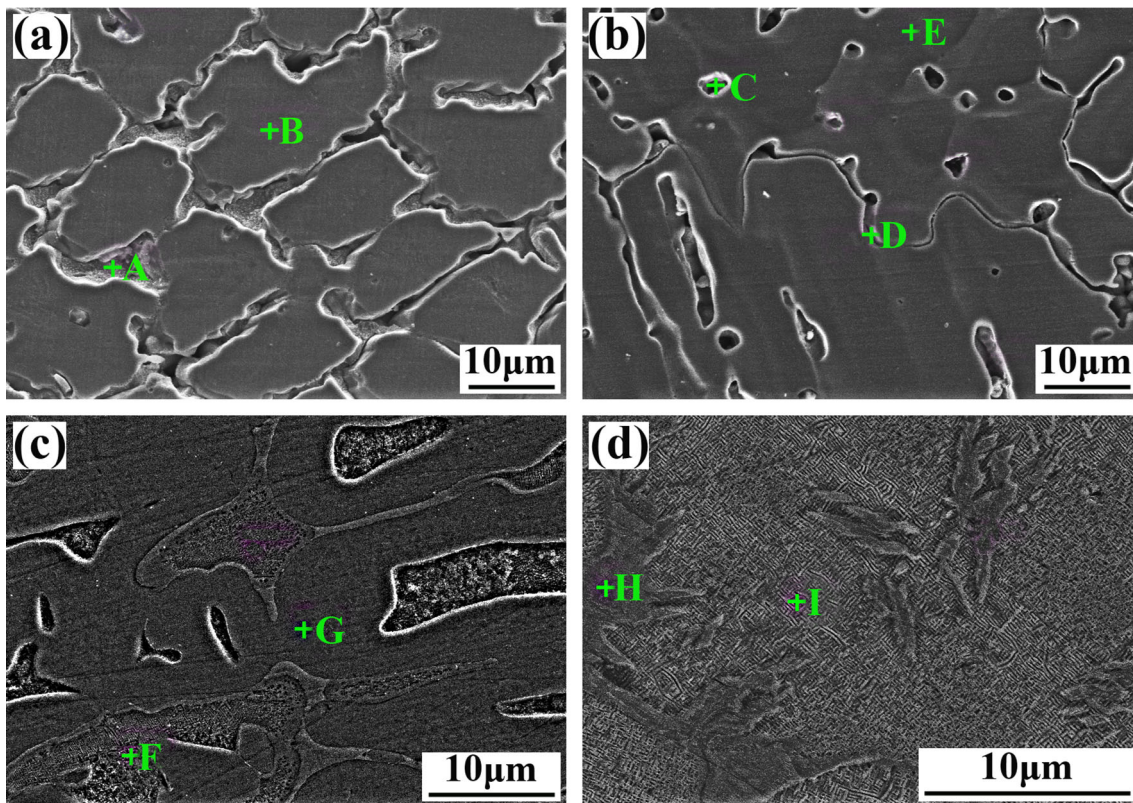


Fig. 5 Typical microstructures in three types of WZs: (a) Sample 1; (b) Sample 2; (c, d) Sample 3

Fig. 5(a). The results of EDS point analysis in Table 2 indicate that the content of Cu element in the grain boundaries (see A-point) is much higher than that in the equiaxed dendritic grains (see B-point). It implies that the segregation of Cu element along the grain boundaries is presented in the WZ of Sample 1.

For the WZ of Sample 2, the evolution of grain morphologies is shown in Fig. 6(a), (c) and (d). Cellular crystals are observed in almost all of the WZ, which is different from the equiaxed dendritic grains and fine columnar grains in Sample 1. Figure 5(b) presents the SEM image of the cellular crystals in Sample 2. The EDS results in Table 2 imply that the amount of Al in the WZ of Sample 2 (see the measured points of C, D, and E) is higher than that of Sample 1. Moreover, the content of Cu element in the grain boundaries of Sample 2 (see D-point) is sharply decreased compared to that of Sample 1 (see A-point).

Table 2 Element content, at.% in the measured point in three types of WZs

Samples	Measured point	Fe	Ni	Cu	Al	Cr
Sample 1	A	12.4	12.1	66.8	6.0	2.7
	B	48.2	23.6	12.2	3.5	12.6
Sample 2	C	26.9	23.0	32.7	12.5	4.9
	D	43.1	22.2	15.2	10.4	9.2
	E	53.0	19.7	8.9	7.2	11.2
Sample 3	F	34.3	23.4	12.3	18.0	11.9
	G	45.3	21.7	9.3	9.8	14.0
	H	30.0	26.7	18.4	14.5	10.4
	I	26.5	27.6	17.5	18.6	9.8

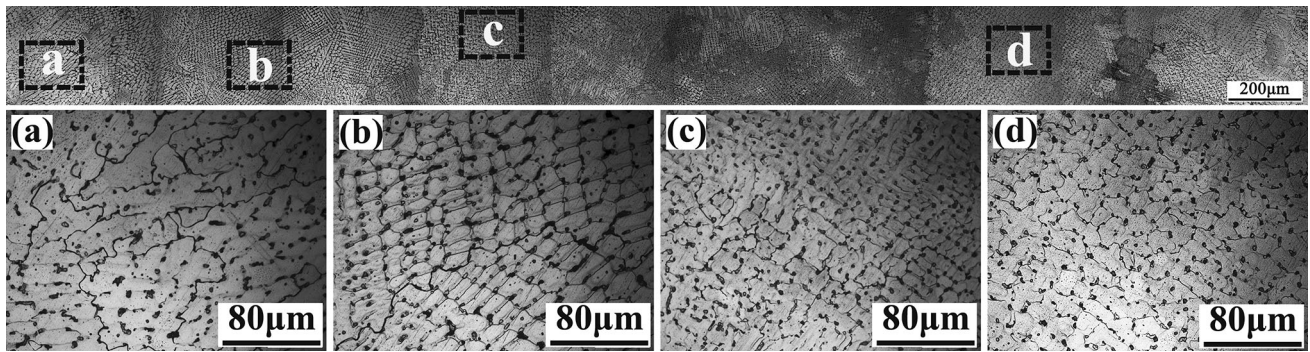


Fig. 6 Microstructures evolution of the WZ of Sample 2: (a) WZ on the left side; (b, c) the WZ inside; (d) WZ on the right side

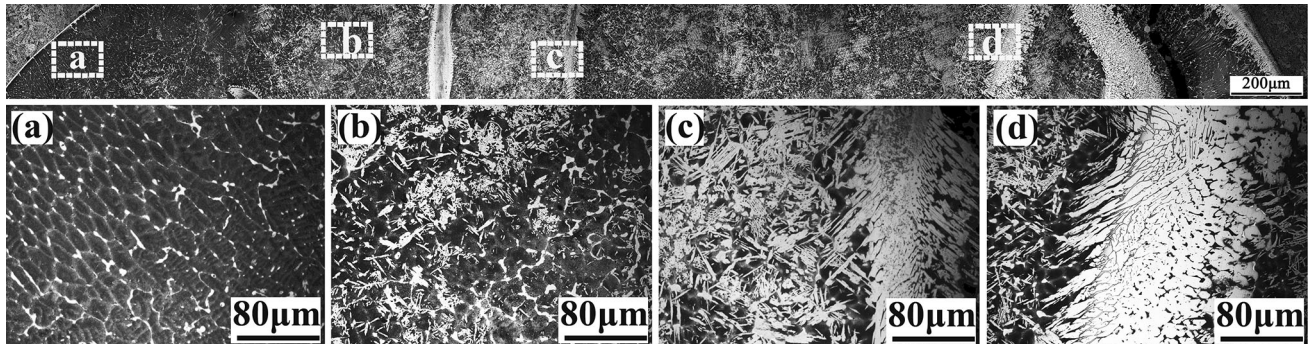


Fig. 7 Microstructures evolution of the WZ of Sample 3: (a) columnar grains on the left side of the WZ; (b, c) spinodal decomposition structures on the WZ inside; (d) columnar grains on the right side of the WZ

The differences in Cu content between intragranular and intergranular are significantly reduced. It means that increasing Al content in the multi-principal alloy wires could alleviate the segregation of Cu element along the grain boundaries in the WZ.

The microstructure evolution on the cross section of WZ for Sample 3 is presented in Fig. 7. Columnar grains are observed on the left side of WZ near the BM/WZ interface. The width of the region with the columnar grains is $\sim 200 \mu\text{m}$ in the TD. Spinodal decomposition structures are observed in most regions of the WZ for Sample 3. Spinodal decomposition structures could be easily found in HEAs with a supersaturated solid solution, especially for the alloys during the rapid cooling process (Ref 24, 43). Moreover, some narrow regions with a width of $60 \sim 150 \mu\text{m}$ having columnar microstructures are also observed in the WZ. The columnar grains and spinodal decomposition structures have been examined by SEM and EDS (see Fig. 5c and d, respectively). It is seen that the Fe content in the columnar microstructures is approximate 45 at.% (see G-point), which is significantly higher than spinodal decomposition structures (see I-point). The content of each element in the spinodal decomposition structures is within the range of $10 \sim 35$ at.%. It is noted that the content of all elements in WZ of Sample 3 is well-consistent with the definition of HEAs.

Figure 8 presents that FCC phase structures are detected in the WZs for both Samples 1 and 2. Moreover, two sub-peaks are presented in the highest peak for the XRD pattern of Sample 1. The highest peak of Sample 1 is magnified and illustrated in the small figure in Fig. 8. The two sub-peaks were identified as FCC and Cu, respectively. It means that the characteristic peaks

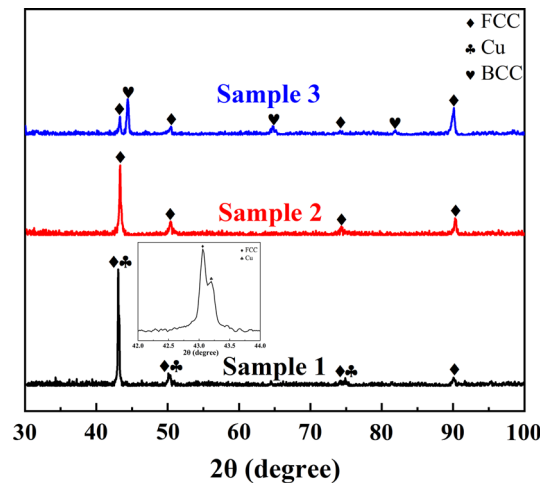


Fig. 8 XRD pattern of three types of WZs

of Cu phase are identified in Sample 1. The reason is mainly related to a high binary mixing enthalpy of Cu and other elements (such as Fe, Ni, and Cr), which results in the segregation of Cu element along the grain boundaries and causes the formation of the Cu phase in the XRD pattern of Sample 1. Similar results are widely reported that the characteristic peaks of Cu phase are identified separately in Cu-containing HEAs (Ref 15, 44). Owing to the low binary mixing enthalpies of Al and Fe, Cr, Ni elements, the more Al element in WZs of Samples 2 and 3 could reduce the mixing enthalpy. Therefore, no characteristic peak of Cu phase is found in the

XRD patterns of Samples 2 and 3. Figure 8 indicates that FCC + BCC dual-phase structures are detected in the WZ for Sample 3. And the BCC phase is the ordered BCC phase (B2) structure. Based on the relative height of the diffraction peak, it is measured that the volume fraction ratio of BCC and FCC phases is about 2.07: 1 for the WZ of Sample 3. The results indicate that an increase in the Al content of the multi-principal alloy wires can promote the generation of the BCC phase. As the Al content reaches 26 at.% in the filler wires, the phase structures in the WZs can transform from FCC single phase to FCC + BCC dual phases. The results are well-consistent with previous studies (Ref 30, 32).

3.3 Microhardness

Figure 9 shows that the BM of Q235 steel has a mean hardness of ~ 120 HV, while the BM of 304 stainless steel shows a hardness of ~ 200 HV. The hardness of Sample 1 is ~ 185 HV, which is slightly lower than that of Sample 2 (~ 195 HV). The hardness values of Samples 1 and 2 are higher than the BM of Q235 steel. However, a rapid increase in hardness is presented in Sample 3 compared to Samples 1 and 2, which reach ~ 395 HV. Li et al. (Ref 36) found that the hardness of the WZ of L415/316L bimetal pipes is ~ 225 HV, which is mainly ascribed to the low content of C element in the welding wire ER309L. It is also reported that the hardness value of the WZ can reach ~ 425 HV by using carbon steel filler material. The reason is mainly attributed to the formation of martensite in the WZ by using carbon steel filler material (Ref 36). In this study, the hardness values of Samples 1 and 2 are similar to that of the WZ by using stainless steel filler material, while the hardness value of Sample 3 is similar to that of the WZ by using carbon steel filler material in the previous study (Ref 36). However, the microstructures and the elemental composition in WZs in this study are different from the previous studies (Ref 35, 36). It should be noted that martensite structure has not been achieved in the WZ of Sample 3, which still displays an extremely high hardness. The increased hardness in Sample 3 is mainly ascribed to the formation of BCC phase structures (see Fig. 8).

3.4 Tensile Properties

The engineering stress–strain curves of various samples are provided in Fig. 10(a). It is seen that all the welded joints

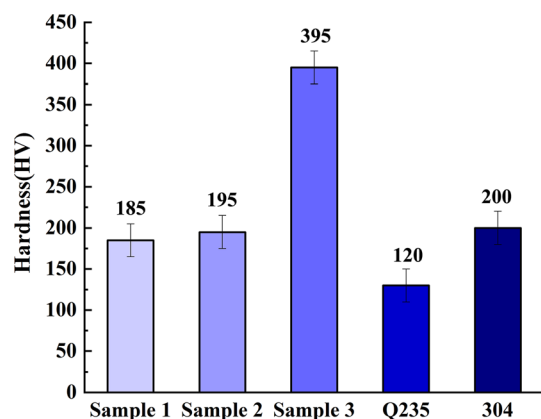


Fig. 9 Mean hardness values on the cross section of three types of WZs as well as the BMs of Q235 steel and 304 stainless steel

possess lower tensile strengths than the BM sample (~ 568 MPa). It is also confirmed by the fracture positions of the welded joints, which are not fractured in the BM but WZs (see Fig. 10b). Figure 10(a) indicates the lowest ultimate tensile strength of 379 MPa presented in Sample 1. The ultimate tensile strength of Sample 3 (~ 528 MPa) is higher than that of Sample 2 (~ 488 MPa). Moreover, the elongations of the three types of welded joints are much lower than that of the BM sample. And the elongations are increased from Sample 1 to Sample 3. It means that the improvement of joint mechanical properties is observed from Sample 1 to Sample 3. It is well-consistent with the trends of hardness values in those WZs. Several reasons may attribute to this result. Firstly, the key factor is related to the increasing Al content in the filler wires. As shown in Fig. 8, increasing Al content can promote the formation of BCC structure in the WZ, which causes the phase structures in the WZs changed from FCC structures to FCC + BCC structures. As a result, the hardness values in WZs and the tensile strength of the joints are significantly improved. Similar results have been widely reported in many Al-containing HEAs (Ref 26, 45). Secondly, increasing the content of Al element will inevitably lead to a decrease in the content ratio of the other four elements. Therefore, the changes in the joint mechanical properties may have some relationship with the content ratio of the other four elements in the WZs, especially for Cu element. As indicated in Fig. 8 and Table 2, owing to the relatively high content of Cu element in the WZ of Sample 1, the formation of the Cu phase is found in Sample 1. Moreover, the segregation of Cu element along the grain boundaries is presented in the WZ of Sample 1, which significantly reduces the tensile strength and elongation of Sample 1 compared to that of Samples 2 and 3.

Figure 11 presents that a clean rock-sugar-like fracture is observed on the plane of TD—welding direction (WD). Typical brittle fracture morphologies are found for those three types of welded samples. Microstructures near the fracture positions are analyzed to investigate the fracture behavior of three types of welded joints (see Fig. 12). An intergranular fracture along the equiaxed dendritic grains is observed for Sample 1 (see Fig. 12d). The reason may have a close relationship with the segregation of Cu element for Sample 1 (see Table 2). Previous studies (Ref 19, 31) indicated that the segregation of Cu element can result in low strength and plasticity in grain boundaries and finally fracture along the grain boundaries. Figure 12(b) and (c) present that both Samples 2 and 3 fractured in the columnar grain regions. And transgranular fractures are observed in those two samples. The reduced segregation of Cu element is the main reason for the results.

4. Discussion

Due to the cocktail effect of HEAs, the composition changing and alloying in multi-principal filler materials is expected to control the mechanical properties of welded joints. Three types of Cr-Ni-Cu-Al multi-principal alloy wires were used in this study to investigate the microstructure evolution and mechanical properties of the welded joints. It is first critical to create the high-entropy environment in the WZs by using the multi-principal alloy wires. Previous studies reported that physicochemical parameters, such as entropy of mixing (ΔS_{mix}) and enthalpy of mixing (ΔH_{mix}), could be used to evaluate the

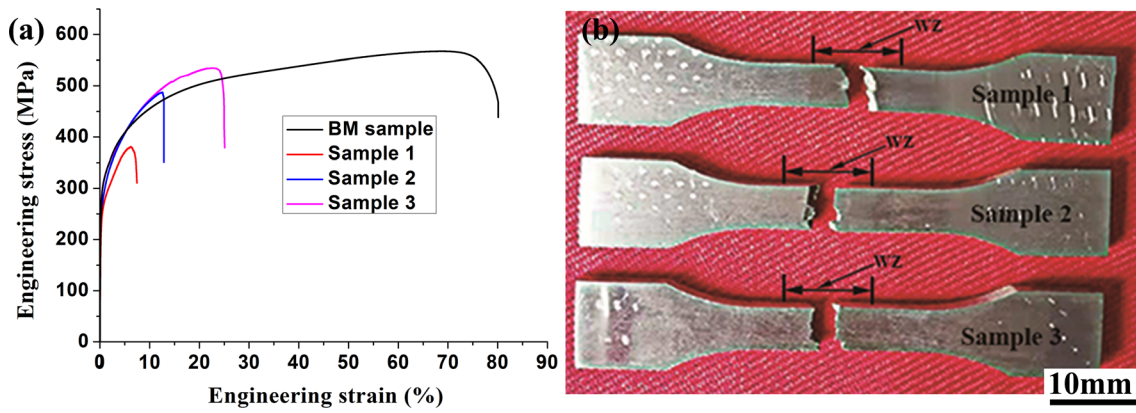


Fig. 10 Tensile properties and fracture positions of three types of welded joints: (a) the stress–strain curves; (b) fracture positions

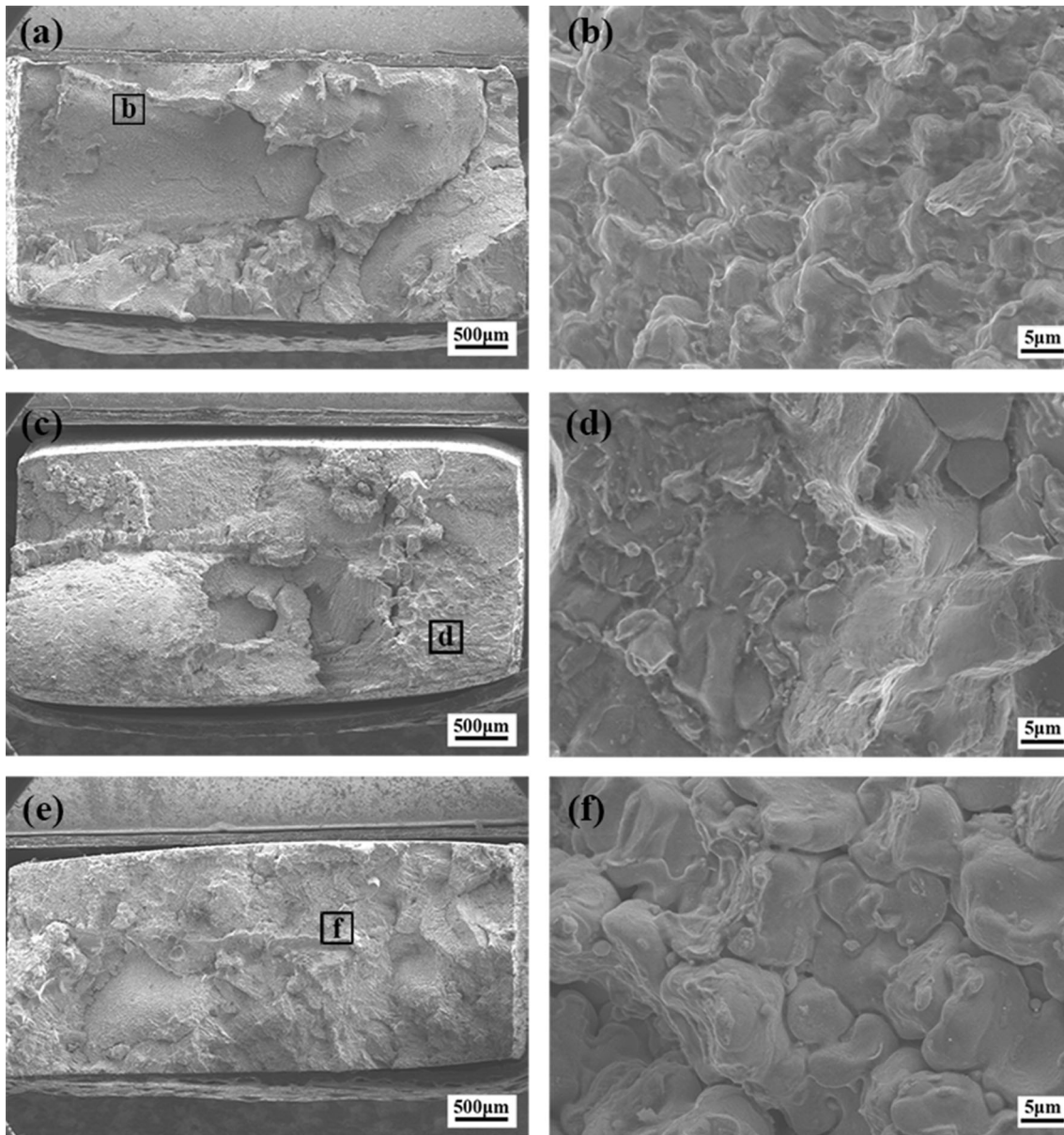


Fig. 11 Fracture surfaces of the welded joints of 304/Q235 stainless steel clad sheets by using the multi-principal alloy wires of Cr-Ni-Cu-Al: (a, b) Sample 1; (c, d) Sample 2; (e, f) Sample 3

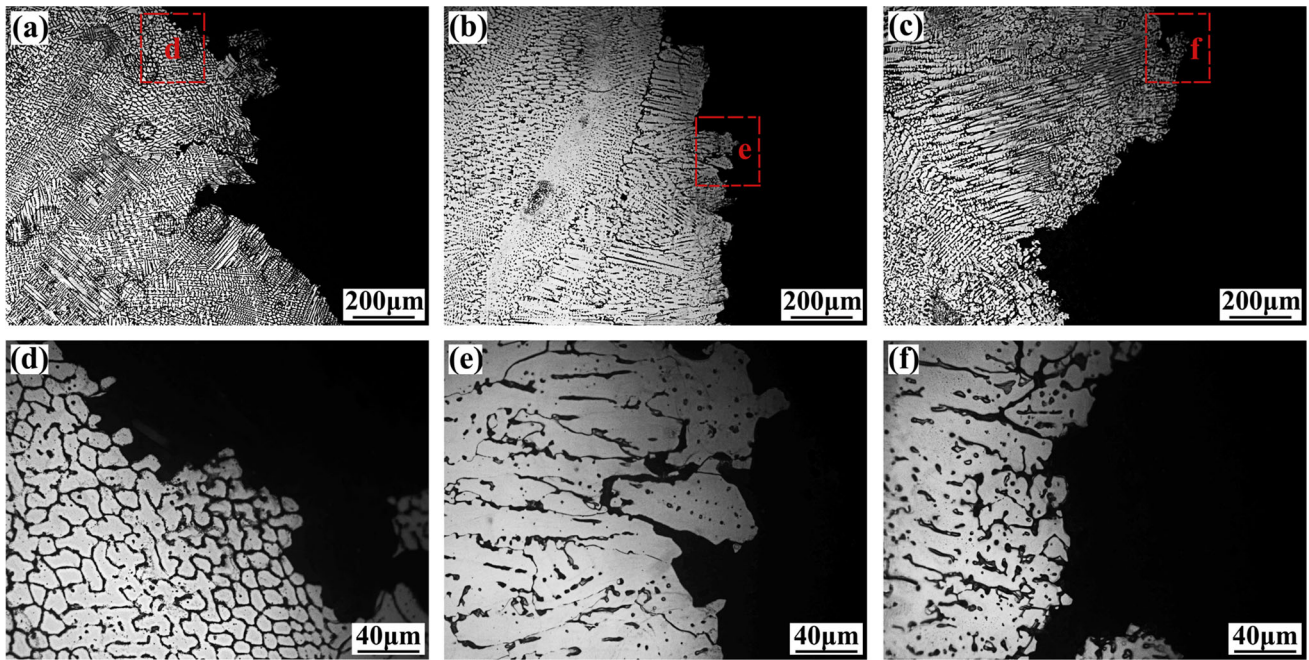


Fig. 12 Microstructures near the fracture line of the welded joints of 304/Q235 stainless steel clad sheets by using the multi-principal alloy wires of Cr-Ni-Cu-Al: (a, d) Sample 1; (b, e) Sample 2; (c, f) Sample 3

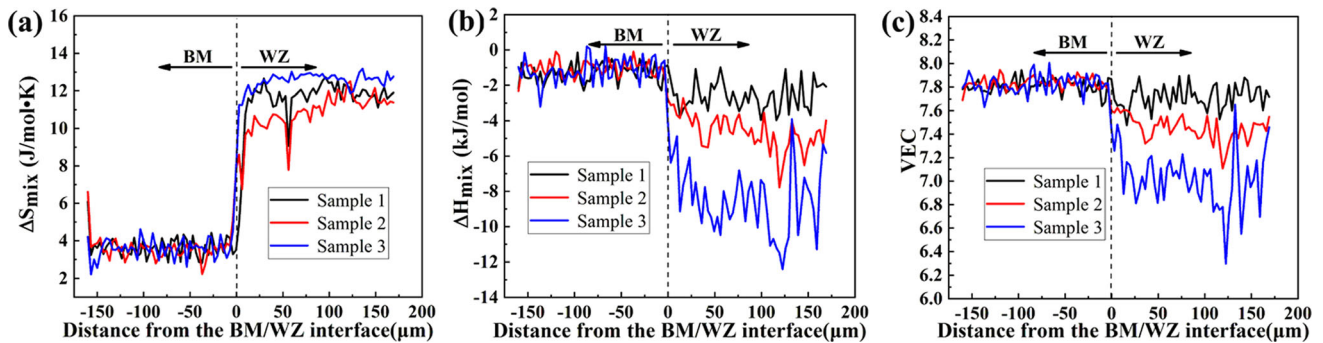


Fig. 13 Variation of some physical parameters from the BM to the WZ in three types of welded joints: (a) the ΔS_{mix} ; (b) the ΔH_{mix} ; (c) the VEC

thermophysical characteristics of HEAs (Ref 46, 47). The parameters are calculated based on the elemental composition and the binary mixing enthalpies. It is seen as follows:

$$\Delta S_{\text{mix}} = -R \sum_{i=1}^n (c_i \ln c_i) \quad (\text{Eq 1})$$

$$\Delta H_{\text{mix}} = \sum_{i=1}^n \Omega_{ij} c_i c_j \quad (\text{Eq 2})$$

Here, c_i and c_j are the molar percentages of elements i and j in HEAs, respectively. Ω_{ij} is calculated as four times the binary alloy mixing enthalpies, and R is the gas molar constant (8.314 J/(mol·K)) (Ref 46, 47).

The distribution curves of ΔS_{mix} and ΔH_{mix} from the BM to the WZs for those three types of welded joints are calculated based on the EDS line scanning results in Fig. 3. Figure 13(a) shows that the value of ΔS_{mix} in the BM is 3 ~ 4 J/(mol·K), while that of the WZs is 10 ~ 13 J/(mol·K). Attributed to the multi-principal alloy wires, a large amount of Cr, Ni, Cu, and Al elements are presented in the WZs, significantly enhancing

the values of ΔS_{mix} in the WZs. Moreover, Fig. 13(a) indicates the value of ΔS_{mix} for Sample 3 is larger than 1.5R, which is well-consistent with the definition of HEAs. However, the values of ΔS_{mix} for Samples 1 and 2 are less than 1.5R, especially for the regions close to the BM/WZ interface. Samples 1 and 2 are more accurately considered as medium-entropy alloys rather than HEAs. The reason is mainly related to the high dilution rate, resulting in a large amount of Fe introduced into the molten pool (see Fig. 3). The chemical composition of the WZs near the BM/WZ interface deviates from that of HEAs.

Figure 13b presents that the value of ΔH_{mix} is gradually decreased from the BM to the WZ. Moreover, Fig. 13(a) and (b) indicates that the value of ΔS_{mix} in the WZ for Sample 3 is slightly higher than that of Samples 1 and 2, while the value of ΔH_{mix} in the WZ for Sample 3 is lower than the other two samples. The results indicate that with the increasing Al content in the filler wires, the value of ΔS_{mix} in the WZ is slightly increased, while the value of ΔH_{mix} is significantly decreased.

Based on the formula of the Gibbs free energy (ΔG_{mix}), $\Delta G_{\text{mix}} = \Delta H_{\text{mix}} - T\Delta S_{\text{mix}}$, as well as the results in Fig. 13(a) and (b), the value of ΔG_{mix} in the WZs would be significantly decreased compared to the BM. In addition, the value of ΔG_{mix} in the WZs would be gradually decreased by increasing the Al content in the filler wires. Previous studies suggested that the low value of ΔG_{mix} in multi-principal alloys could easily accelerate the generation of solid-solution structures (Ref 46, 48). FCC solid-solution phase is detected in Samples 1 and 2 in this study. FCC + BCC dual-phase structures are observed in the WZ for Sample 3. In addition to the appropriate element contents in the WZs, especially for Sample 3 (see Fig. 3f), it could be concluded that using the Cr-Ni-Cu-Al multi-principal alloy wires can promote the generation of a high (medium)-entropy environment in the WZs.

The Al content has an impact on the phase structures in HEAs. Tong et al. (Ref 49) found that a BCC structure is gradually formed in $\text{Al}_x\text{CoCrCuFeNi}$ alloys when the value of x reached 0.8. A single BCC phase structure can be achieved when the content of Al element is larger than $x = 2.8$. Stepanov et al. (Ref 50) found that a single FCC phase structure is formed in the CoCrFeMnNi-Al alloys with a low Al content. It is expected to form BCC phase structure at the Al content over 6 at.%. Moreover, the FCC phase structure would eliminate as the Al content reached 17 at.%. In this study, Fig. 8 indicates that by increasing the Al content, the phase structures in the WZs are transformed from the FCC phase into BCC + FCC phases, especially for the Al content in the filler wires reached 26 at.%. Moreover, it should be noted that the Cu content has also an impact on the phase structures in HEAs. In the present study, the amount of Al pure wires is increased, while keeping the constant amount of other pure or alloy wires during the manufacturing of multi-principal alloy wires. Therefore, increasing the ratio of Al content will inevitably reduce the content ratio of the other four elements. As is known, the binary mixing enthalpy between Cu and Fe, Ni, and Cr elements is 13 kJ/mol, 12 kJ/mol, and 4 kJ/mol, respectively (Ref 48). For Sample 1, the high content of Cu element leads to the phase separation and the formation of the Cu phase in Sample 1. With the increase in Al content, the content ratio of Cu decreases, leading to the decrease in the value of ΔH_{mix} in the WZs for Samples 2 and 3 (see Fig. 13b). Then, no characteristic peak of Cu phase is found in the XRD patterns of Samples 2 and 3 (see Fig. 8). Moreover, according to previous studies (Ref 32, 42), valence electron concentration (VEC) is a critical factor to decide the BCC or FCC structures in HEAs. Guo et al. (Ref 48) suggested that FCC + BCC phases are formed in HEAs as the VEC value is between 6.87 and 8. And the lower value of VEC can promote the formation of BCC structure. The variations of VEC from the BM to the WZs are shown in Fig. 13(c). A decrease in the value of VEC is observed in the WZs as the increase in Al content in the filler wires, which is well-consistent with the generation of BCC phase in the WZ of Sample 3.

Previous studies reported that the hardness and tensile strength have a strong correlation with the Al content in the Al-containing HEAs (Ref 31, 32). Xu et al. (Ref 30) found that increasing Al content in $\text{Al}_x\text{CrMnFeCoNi}$ alloys can promote

the formation of BCC phase and cause a decrease in the size of FCC grains. It results in remarkably improved tensile strength. Stepanov et al. (Ref 50) found that increasing the content of Al element from 0 to 10 at.% can improve the compression properties of $\text{Fe}_{40}\text{Mn}_{25}\text{Cr}_{20}\text{Ni}_{15-x}\text{Al}_x$ alloys. Further increasing the Al content has not affected strength noticeably. The reason is mainly related to the constant fraction of BCC phases. In the present study, as the Al content reaches 26 at.% in the filler wires, the phase structures in the WZs are transformed from the FCC phases to the FCC + BCC phases. Therefore, a sharp increase in the hardness is presented in the WZ of Sample 3 (~ 395 HV). And the ultimate tensile strength is significantly increased from Sample 1 (~ 379 MPa) to Sample 3 (~ 528 MPa). The phase structure transformed from FCC into BCC would be the main reason for the results.

Moreover, it should be noted that owing to the high dilution rate, a large amount of Fe element is introduced into the molten pool, resulting in the high content of Fe element (44.3 \sim 49.2 at.%) in the WZs of Samples 1 and 2, especially for the regions near close to the BM/WZ interface. It deviates from the chemical composition of HEAs. The issue has an adverse effect on mechanical properties. Therefore, controlling the dilution during welding is of great concern to adjust the mechanical properties of the welded joints by using multi-principal filler materials. There are several methods to control the weld dilution. Firstly, selecting the appropriate shape and angle of the groove is an important effective method to control weld dilution (Ref 51). Secondly, controlling the welding heat input is another effective method to reduce the weld dilution. Advanced fusion welding methods such as Cold Metal Transfer (CMT) may be an ideal choice to reduce the weld dilution during the welding of multi-principal filler materials, which would be an interesting research direction in the future.

5. Conclusions

1. With the increasing Al content of the multi-principal filler wires, the grain morphologies in the WZs were changed from columnar/dendritic grains to spinodal decomposition structures.
2. An increase in the Al content could promote the generation of the BCC phase in the WZs. The phase structures in the WZs were changed from the FCC phases into the FCC + BCC phases as the Al content of the filler wires reached 26 at.%.
3. As the Al content in the filler wires reached 26 at.%, the hardness of the WZs was increased by ~ 2 times. The ultimate tensile strength of the joints was improved from 379 MPa to ~ 528 MPa.
4. Three types of welded samples were fractured in the WZs and showed the rock-sugar-like fracture morphologies. An intergranular fracture was observed for Sample 1, while transgranular fractures were seen in the other two samples.

Acknowledgments

This study was financially supported by National Natural Science Foundation of China (51805171, 51965022), Natural Science Foundation of Jiangxi Province (20192BAB206028), Graduate Innovation Foundation Project of Jiangxi Province (YC2021-S428).

Data Availability Research data are not shared.

Conflict of interest

The authors declare that they have no known competing financial interests or personal relationships that could have appeared to influence the work reported in this paper.

References

1. K. Zhou, J. Li, L. Wang, H. Yang, Z. Wang and J. Wang, Direct Laser Deposited Bulk CoCrFeNiNb_x High-Entropy Alloys, *Intermetallics*, 2019, **114**, 106592. <https://doi.org/10.1016/j.intermet.2019.106592>
2. A. Ghaderi, H. Moghanni and K. Dehghani, Microstructural Evolution and Mechanical Properties of Al_{0.5}CoCrFeNi High-Entropy Alloy After Cold Rolling and Annealing Treatments, *J. Mater. Eng. Perform.*, 2021, **30**, p 7817–7825. <https://doi.org/10.1007/s11665-021-05886-y>
3. W. Wu, W. Liang, S. Guan, R. Wei and Z. Ning, A Novel Hypoeutectic High-Entropy Alloy CrFe₂Ni₂Mo_{0.3}Nb_{0.25} with High Tensile Strength and Good Ductility, *J. Mater. Eng. Perform.*, 2022 <https://doi.org/10.1007/s11665-022-06881-7>
4. D. Castro, P. Jaeger, A.C. Baptista and J.P. Oliveira, An Overview of High-Entropy Alloys as Biomaterials, *Metals*, 2021, **11**, p 648. <https://doi.org/10.3390/met11040648>
5. J.G. Lopes and J.P. Oliveira, A Short Review on Welding and Joining of High Entropy Alloys, *Metals*, 2020, **10**, p 212. <https://doi.org/10.3390/met10020212>
6. M. Rhode, T. Richter, D. Schroepfer, A.M. Manzoni, M. Schneider and G. Laplanche, Welding of High-Entropy Alloys and Compositionally Complex Alloys- an Overview, *Weld World*, 2021, **65**, p 1645–1659. <https://doi.org/10.1007/s40194-021-01110-6>
7. H. Nam, B. Moon, S. Park, N. Kim, S. Song, N. Park, Y. Na and N. Kang, Gas Tungsten Arc Weldability of Stainless Steel 304 Using CoCrFeMnNi Filler Metals for Cryogenic Applications, *Sci. Technol. Weld. Joi.*, 2021, **27**, p 33–42. <https://doi.org/10.1080/13621718.2021.1996851>
8. H. Li, W. Shen, W. Chen, W. Wang, G. Liu, C. Lu, W. Zheng, Y. Ma, J. Yang, Z. Ding, H. Zou and Y. He, Microstructural Evolution and Mechanical Properties of AlCoCrFeNi High-Entropy Alloy Joints Brazed Using a Novel Ni-Based Filler, *J. Alloy Compd.*, 2021, **860**, 157926. <https://doi.org/10.1016/j.jallcom.2020.157926>
9. G. Wang, G. Sheng, Q. Yu, J. Sun, R. Li and X. Yuan, Investigation on Regulating Inter-Granular Penetration in CoCrMnFeNi High-Entropy Alloy and 304 Stainless Steel Dissimilar Joints, *Mater. Sci. Eng. A*, 2021, **800**, 140291. <https://doi.org/10.1016/j.msea.2020.140291>
10. Y.J. Du, J.T. Xiong, F. Jin, S.W. Li, L. Yuan, D. Feng, J.M. Shi and J.L. Li, Microstructure Evolution and Mechanical Properties of Diffusion Bonding Al₅(TiZrHfNb)_{0.5} Refractory High Entropy Alloy to Ti₂AlNb Alloy, *Mater. Sci. Eng. A*, 2021, **802**, 140610. <https://doi.org/10.1016/j.msea.2020.140610>
11. J. Li, X. Meng, L. Wan and Y. Huang, Welding of High Entropy Alloys: Progresses, Challenges and Perspectives, *J. Manuf. Process.*, 2021, **68**, p 293–331. <https://doi.org/10.1016/j.jmapro.2021.05.042>
12. J.P. Oliveira, J. Shen, Z. Zeng, J.M. Park, Y.T. Choi, N. Schell, E. Maawad, N. Zhou and H.S. Kim, Dissimilar Laser Welding of a CoCrFeMnNi High Entropy Alloy to 316 Stainless Steel, *Scripta Mater.*, 2022, **206**, 114219. <https://doi.org/10.1016/j.scriptamat.2021.114219>
13. J. Oliveira, A. Shamsolhodaei, J. Shen, J. Lopes, R. Gonçalves, M. de Brito Ferraz, L. Piçarra, Z. Zeng, N. Schell and N. Zhou, Improving the Ductility in Laser Welded Joints of CoCrFeMnNi High Entropy Alloy to 316 Stainless Steel, *Mater. Des.*, 2022, **219**, p 110717. <https://doi.org/10.1016/j.matdes.2022.110717>
14. J.P. Oliveira, T.M. Curado, Z. Zeng, J.G. Lopes, E. Rossinyol, J.M. Park, N. Schell, F.M. Braz Fernandes and H.S. Kim, Gas Tungsten Arc Welding of as-Rolled CrMnFeCoNi High Entropy Alloy, *Mater. Des.*, 2020, **189**, p 108505. <https://doi.org/10.1016/j.matdes.2020.108505>
15. A.C. Martin, J.P. Oliveira and C. Fink, Elemental Effects on Weld Cracking Susceptibility in Al_xCoCrCu₂FeNi High-Entropy Alloy, *Metall. Mater. Trans. A*, 2019, **51**, p 778–787. <https://doi.org/10.1007/s11661-019-05564-8>
16. Y. Yang, G. Wang, R. He, D. Shu, C. Tan and W. Cao, Microstructure and Mechanical Properties of ZrB₂-SiC/Nb Joints Brazed with CoFeNiCrCuTi_x High-Entropy Alloy Filler, *J. Am. Ceram. Soc.*, 2021, **104**, p 2992–3003. <https://doi.org/10.1111/jace.17732>
17. D. Luo, Y. Xiao, L. Hardwick, R. Snell, M. Way, X. Sanuy Morell, F. Livera, N. Ludford, C. Panwisawas, H. Dong and R., Goodall, High Entropy Alloys as Filler Metals for Joining, *Entropy*, 2021, **23**, p 78. <https://doi.org/10.3390/e23010078>
18. P. Li, H. Sun, H. Dong, Y. Xia, S. Wang and X. Hao, Microstructural Evolution, Bonding Mechanism and Mechanical Properties of AlCoCrFeNi_{2.1} Eutectic High Entropy Alloy Joint Fabricated Via Diffusion Bonding, *Mater. Sci. Eng. A*, 2021, **814**, p 141211. <https://doi.org/10.1016/j.msea.2021.141211>
19. X. Hao, H. Dong, Y. Xia and P. Li, Microstructure and Mechanical Properties of Laser Welded TC4 Titanium Alloy/304 Stainless Steel Joint with (CoCrFeNi)_{100-x}Cu_x High-Entropy Alloy Interlayer, *J. Alloy Compd.*, 2019, **803**, p 649–657. <https://doi.org/10.1016/j.jallcom.2019.06.225>
20. D. Liu, R. Guo, Y. Hu, J. Zeng, M. Shen, Y. Tang, H. Jiao, L. Zhao and X. Nie, Effects of the Elemental Composition of High-Entropy Filler Metals on the Mechanical Properties of Dissimilar Metal Joints Between Stainless Steel and Low Carbon Steel, *J. Mater. Res. Technol.*, 2020, **9**, p 11453–11463. <https://doi.org/10.1016/j.jmrt.2021.04.060>
21. D. Liu, R. Guo, Y. Hu, M. Shen, Y. Tang, L. Zhao, D. Li and X. Wang, Dissimilar Metal Joining of 304 Stainless Steel to SMA490BW Steel Using the Filler Metal Powders with a High-Entropy Design, *Met. Mater. Int.*, 2020, **26**, p 854–866. <https://doi.org/10.1007/s12540-019-00400-5>
22. D. Liu, J. Wang, M. Xu, H. Jiao, Y. Tang, D. Li, L. Zhao and S. Han, Evaluation of Dissimilar Metal Joining of Aluminum Alloy to Stainless Steel Using the Filler Metals with a High-Entropy Design, *J. Manuf. Process.*, 2020, **58**, p 500–509. <https://doi.org/10.1016/j.jmapro.2020.08.031>
23. A. Vyas, J. Menghani and H. Natu, Influence of WC Particle on the Metallurgical, Mechanical, and Corrosion Behavior of AlFeCuCrCoNi-WC_x High-Entropy Alloy Coatings, *J. Mater. Eng. Perform.*, 2021, **30**, p 2449–2461. <https://doi.org/10.1007/s11665-021-05523-8>
24. Z. Tian, Y. Zhao, Y. Jiang, H. Ren and C. Qin, Investigation of Microstructure and Properties of FeCoCrNiAlMo_x Alloy Coatings Prepared by Broadband-Beam Laser Cladding Technology, *J. Mater. Sci.*, 2020, **55**, p 4478–4492. <https://doi.org/10.1007/s10853-019-04275-0>
25. Y. Lu, Y. Dong, H. Jiang, Z. Wang, Z. Cao, S. Guo, T. Wang, T. Li and P.K. Liaw, Promising Properties and Future Trend of Eutectic High Entropy Alloys, *Scripta Mater.*, 2020, **187**, p 202–209. <https://doi.org/10.1016/j.scriptamat.2020.06.022>
26. J. Joseph, N. Stanford, P. Hodgson and D.M. Fabijanic, Understanding the Mechanical Behaviour and the Large Strength/Ductility Differences Between FCC and BCC Al_xCoCrFeNi High Entropy Alloys, *J. Alloy Compd.*, 2017, **726**, p 885–895. <https://doi.org/10.1016/j.jallcom.2017.08.067>
27. K.B. Zhang, Z.Y. Fu, J.Y. Zhang, W.M. Wang, H. Wang, Y.C. Wang, Q.J. Zhang and J. Shi, Microstructure and Mechanical Properties of CoCrFeNiTiAl_x High-Entropy Alloys, *Mater. Sci. Eng. A*, 2009, **508**, p 214–219. <https://doi.org/10.1016/j.msea.2008.12.053>
28. Z. Wang, X. Wang, H. Yue, G. Shi and S. Wang, Microstructure, Thermodynamics and Compressive Properties of AlCoCrCuMn-x (x=Fe, Ti) High-Entropy Alloys, *Mater. Sci. Eng. A*, 2015, **627**, p 391–398. <https://doi.org/10.1016/j.msea.2015.01.002>
29. L. Jiang, Z.Q. Cao, J.C. Jie, J.J. Zhang, Y.P. Lu, T.M. Wang and T.J. Li, Effect of Mo and Ni Elements on Microstructure Evolution and Mechanical Properties of the CoFeNi₂VMo_y High Entropy Alloys, *J. Alloy Compd.*, 2015, **649**, p 585–590. <https://doi.org/10.1016/j.jallcom.2015.07.185>

30. J. Xu, C.-M. Cao, P. Gu and L.-M. Peng, Microstructures, Tensile Properties and Serrated Flow of Al CrMnFeCoNi High Entropy Alloys, *T. Nonferr. Metal. Soc.*, 2020, **30**, p 746–755. [https://doi.org/10.1016/S1003-6326\(20\)65250-5](https://doi.org/10.1016/S1003-6326(20)65250-5)
31. P. Wang, X. Cheng, H. Cai, Y. Xue and Y. Zhang, Influence of Increasing Al Concentration on Phase, Microstructure and Mechanical Behaviors of Ni_{1.5}CoFeCu_{1-x}Al_xV_{0.5} High Entropy Alloys, *Mater. Sci. Eng. A*, 2017, **708**, p 523–536. <https://doi.org/10.1016/j.msea.2017.09.119>
32. D.B. Miracle and O.N. Senkov, A Critical Review of High Entropy alloys and Related Concepts, *Acta Mater.*, 2017, **122**, p 448–511. <https://doi.org/10.1016/j.actamat.2016.08.081>
33. M. Zhu, W. Wu, W. Qian, L. Xia, Y. Zhang and B. Wang, A Brief Review on Welding of Stainless Steel Clad Plates: Issues and Future Perspectives, *Int. J. Adv. Manuf. Tech.*, 2021, **115**, p 49–59. <https://doi.org/10.1007/s00170-021-07218-9>
34. G. Ca Li, Y. Tang Qin, B. Zhang, S. Lin and P. Geng, Microstructures and Mechanical Properties of Stainless Steel Clad Plate Joint with Diverse Filler Metals, *J. Mater. Res. Technol.*, 2020, **9**, p 2522–2534. <https://doi.org/10.1016/j.jmrt.2019.12.083>
35. Y. Meng, K. Kang, M. Gao and X. Zeng, Microstructures and Properties of Single-Pass Laser-Arc Hybrid Welded Stainless Clad Steel Plate, *J. Manuf. Process.*, 2018, **36**, p 293–300. <https://doi.org/10.1016/j.jmapro.2018.10.022>
36. L. Li, J. Xiao, B. Han and X. Wang, Microstructure and Mechanical Properties of Welded Joints of L415/316L Bimetal Composite Pipe Using Post Internal-Welding Process, *Int. J. Pres. Ves. Pip.*, 2020, **179**, 104026. <https://doi.org/10.1016/j.ijpvp.2019.104026>
37. Q. An, K.Y. Fan, Y.F. Ge, B.X. Liu, Y.C. Liu, S. Wang, C.X. Chen, P.G. Ji and F.X. Yin, Microstructure and Mechanical Properties of Stainless Steel Clad Plate Joints Produced by TIG and MAG Hybrid Welding, *J. Adhes. Sci. Technol.*, 2019, **34**, p 670–685. <https://doi.org/10.1080/01694243.2019.1677087>
38. A.M. Torbati, R.M. Miranda, L. Quintino, S. Williams and D. Yapp, Optimization Procedures for GMAW of Bimetal Pipes, *J. Mater. Process. Technol.*, 2011, **211**, p 1112–1116. <https://doi.org/10.1016/j.jmatprotec.2011.01.013>
39. W. Huang, H. Wang, T. Rinker and W. Tan, Investigation of Metal Mixing in Laser Keyhole Welding of Dissimilar Metals, *Mater. Des.*, 2020, **195**, 109056. <https://doi.org/10.1016/j.matdes.2020.109056>
40. J.P. Oliveira, Z. Zeng, C. Andrei, F.M. BrazFernandes, R.M. Miranda, A.J. Ramirez, T. Omori and N. Zhou, Dissimilar Laser Welding of Superelastic NiTi and CuAlMn Shape Memory Alloys, *Mater. Des.*, 2017, **128**, p 166–175. <https://doi.org/10.1016/j.matdes.2017.05.011>
41. R. Savinov, Y. Wang and J. Shi, Microstructure and Properties of CeO₂-doped CoCrFeMnNi High Entropy Alloy Fabricated by Laser Metal Deposition, *J. Manuf. Process.*, 2020, **56**, p 1245–1251. <https://doi.org/10.1016/j.jmapro.2020.04.018>
42. Y. Zhang, T.T. Zuo, Z. Tang, M.C. Gao, K.A. Dahmen, P.K. Liaw and Z.P. Lu, Microstructures and Properties of High-Entropy Alloys, *Prog. Mater. Sci.*, 2014, **61**, p 1–93. <https://doi.org/10.1016/j.pmatsci.2013.10.001>
43. L. Huang, X. Wang, X. Zhao, C. Wang and Y. Yang, Analysis on the Key Role in Corrosion Behavior of CoCrNiAlTi-Based High Entropy Alloy, *Mater. Chem. Phys.*, 2021, **259**, 124007. <https://doi.org/10.1016/j.matchemphys.2020.124007>
44. Y.-J. Hsu, W.-C. Chiang and J.-K. Wu, Corrosion Behavior of FeCoNiCrCu_x High-Entropy Alloys in 3.5% Sodium Chloride Solution, *Mater. Chem. Phys.*, 2005, **92**, p 112–117. <https://doi.org/10.1016/j.matchemphys.2005.01.001>
45. X. Sun, H. Zhu, J. Li, J. Huang and Z. Xie, Influence of Aluminum Content on the Microstructure and Properties of the In-Situ TiC Reinforced Al_xFeCoNiCu High Entropy Alloy Matrix Composites, *Mater. Sci. Eng. A*, 2019, **743**, p 540–545. <https://doi.org/10.1016/j.msea.2018.11.120>
46. J.-X. Fu, C.-M. Cao, W. Tong and L.-M. Peng, Effect of Thermomechanical Processing on Microstructure and Mechanical Properties of CoCrFeNiMn High Entropy Alloy, *T. Nonferr. Metal. Soc.*, 2018, **28**, p 931–938. [https://doi.org/10.1016/S1003-6326\(18\)64727-2](https://doi.org/10.1016/S1003-6326(18)64727-2)
47. M.-H. Tsai and J.-W. Yeh, High-Entropy Alloys: A Critical Review, *Mater. Res. Lett.*, 2014, **2**, p 107–123. <https://doi.org/10.1080/21663831.2014.912690>
48. S. Guo and C.T. Liu, Phase Stability in High Entropy Alloys: Formation of Solid-Solution Phase or Amorphous Phase, *Prog. Nat. Sci.*, 2011, **21**, p 433–446. [https://doi.org/10.1016/S1002-0071\(12\)60080-X](https://doi.org/10.1016/S1002-0071(12)60080-X)
49. C.J. Tong, M.R. Chen, J.W. Yeh, S.J. Lin, S.K. Chen, T.T. Shun and S.Y. Chang, Mechanical Performance of the Al_xCoCrCuFeNi High-Entropy Alloy System with Multiprincipal Elements, *Metall. Mater. Trans. A*, 2005, **36**, p 1263–1271. <https://doi.org/10.1007/s11661-005-0218-9>
50. N.D. Stepanov, D.G. Shaysultanov, M.A. Tikhonovsky and S.V. Zharebtsov, Structure and High Temperature Mechanical Properties of Novel Nonequiatomic Fe-(Co, Mn)-Cr-Ni-Al-(Ti) High Entropy Alloys, *Intermetallics*, 2018, **102**, p 140–151. <https://doi.org/10.1016/j.intermet.2018.09.010>
51. D. Liu, W. Wang, X. Zha, R. Guo, H. Jiao and L. Zhao, Effects of Groove on the Microstructure and Mechanical Properties of Dissimilar Steel Welded Joints by Using High-Entropy Filler Metals, *J. Mater. Res. Technol.*, 2021, **13**, p 173–183. <https://doi.org/10.1016/j.jmrt.2021.04.060>

Publisher's Note Springer Nature remains neutral with regard to jurisdictional claims in published maps and institutional affiliations.